Ultra Low-Cycle Fatigue Performance of S420 and S700 Steel Welded Tubular X-joints

Ultra Low-Cycle Fatigue Performance of S420 and S700 Steel Welded Tubular X-joints

Konstantinos Chatziioannou[a], Spyros A. Karamanos[a,b,*], Yuner Huang[a]

[a] *School of Engineering, The University of Edinburgh, Scotland, UK*
[b] *Department of Mechanical Engineering, University of Thessaly, Volos, Greece*

Abstract

The present study is motivated by the need for improving the fatigue performance of offshore wind energy structural systems. In particular, the ultra low-cycle fatigue performance of welded tubular X-joints is examined, motivated by the need of safeguarding the integrity of offshore platforms under extreme loading conditions. The welded specimens are manufactured using hot-rolled tubes of steel grade S420 and S700, and represent X-brace joints of a bottom-fixed offshore wind tubular jacket, with scaling factor of 1:3. Seven specimens are tested under strong fully-reversed cyclic in-plane bending, leading to through-thickness fatigue cracking within less than 100 cycles, simulating extreme loading conditions. The experimental results indicate that X-joints manufactured from both steel grades exhibit similar structural response, in terms of ultra low-cycle fatigue. Rigorous finite element models are also developed, with emphasis on constitutive modeling, to simulate the cyclic loading procedure, providing very good comparisons in terms of load-displacement response and local strain predictions during the initial loading cycles. The experimental data are compared with a large dataset of low-cycle fatigue experiments on welded components, reported in the literature for mild and high-strength steel materials, as well as with existing design provisions. The results indicate similar performance of high-strength steel and mild steel welded connections, and are compared with stress-based and strain-based design methodologies in predicting the number of cycles to failure in the ultra low-cycle fatigue regime.

Keywords: low-cycle fatigue, offshore structures, high-strength steel, welded tubular joints

*Corresponding author
Email address: Spyros.Karamanos@ed.ac.uk (Spyros A. Karamanos)

1. Introduction

Offshore renewable industry is growing rapidly and its industrial targets hit new records every decade [1, 2]. According to the European Wind Energy Association (EWEA) [3], currently, 87.7% of the offshore wind turbines are supported by monopile systems and are located in depths shallower than 25m, while the resulting capacity is less than 4MW. The exploitation of deeper waters and the use of higher output wind turbines require the employment of stiffer and more resilient support systems. Bottom-founded jacket substructures, assembled from tubular welded connections, constitute an attractive solution and characteristic examples of successful installation in depths of 30-45m are, among several others the BEATRICE [4] and Alpha Ventus [5] windfarm parks. The use of offshore wind jackets in depths up to 80m is also under consideration in ongoing research projects [6]. The supporting units are exposed to repeated loading due to ocean waves and the operational loads of the turbine, and may fail due to fatigue at critical locations. The accurate assessment of the fatigue life of jacket substructures is crucial for the sustainability of the project over its design life and it has been the subject of investigation in numerous recent research articles [7, 8, 9].

Welded tubular joints are considered critical structural components of offshore platforms. In particular, their fatigue performance is strongly influenced by the magnitude of the applied cyclic loading. Fatigue failures which are attributed to repeated loading at relatively low stress amplitude are described as high-cycle fatigue and are associated with more than 10^4 load cycles [10]. On the other hand, under extreme cyclic loading, such as severe earthquakes or storm conditions, offshore structural systems and their components are subjected to repeated large inelastic strains. In those extreme cases, failure may occur under a small number of load cycles (less than 100) and is defined as “ultra low-cycle fatigue”, referred to as ULCF. It has been shown experimentally that in welded tubular joints, subjected to repeated inelastic loading, crack initiation and propagation is very fast, leading to stiffness and strength degradation after a relatively small number of cycles [11]. Despite the large number of published work on the high-cycle fatigue of welded tubular joints, the low-cycle fatigue behaviour of such joints has received substantially less attention. Experimental results concerning ultra

low-cycle fatigue tests have been reported in several publications [12, 13, 14] but those tests concern small-scale specimens which may not be able to represent the multiaxial state of stress in welded tubular joints. On the other hand, low-cycle fatigue tests on welded tubular joints have been quite limited, especially for the ULCF regime. An early experimental study concerning tubular X-joints was reported by Baba *et* al. [15]. Welded specimens were tested under low-cycle fatigue loading in an attempt to correlate the induced hot-spot stress range with the number of cycles to failure. The impact of welding defects, size effects and residual stresses was also examined. Thorough investigations have been presented in [16, 17], analysing a large set of experimental data. The studies reported that thickness effects are less pronounced in low-cycle fatigue in comparison to high-cycle fatigue, while a lower mean slope is observed in the logS-logN plot. Additional experimental data were published by Skallerud *et* al. [18] and Scavuzzo *et* al. [19] concerning the low-cycle fatigue performance of tubular welded components. More specifically, Skallerud *et* al. [18] examined experimentally large-scale T-joints, fabricated from seamless pipes with yield strength of 360MPa. Four specimens were tested under intense cyclic axial loading and failure occurred between 7 and 70 load cycles. The ultra low-cycle fatigue endurance was assessed in terms of hot-spot strains and the comparison with the AWS-x curves [20] highlighted the conservativeness of the code. Scavuzzo *et* al. [19] tested 29 carbon steel and 9 stainless steel butt-welded pipes under four-point cyclic bending, leading the specimens to failure within 200-2x10^6 load cycles and providing further information regarding the transition between high-cycle and low-cycle fatigue. A unified design methodology, applicable to high-cycle fatigue and low-cycle fatigue, was recently proposed by Pei and Dong [21] and Pei *et* al. [22], suggesting the use of an equivalent structural strain parameter (ΔE) in combination with a master $\Delta E - N$ curve for assessing the fatigue life of a structural component. Alternatively, an energy-based approach has also been proposed for low-cycle fatigue, that relates the dissipated energy per load cycle to the number of cycles to failure [23, 24].

Another issue related to the construction of offshore structural systems for wind energy production, which attracts increasing attention is the use of high-strength steel. It

should be underlined that until recently, metal alloys of grade up to S355 have been used exclusively in the offshore wind sector. Furthermore, design methodologies for high-cycle fatigue of regular steel welded joints are well established [25, 26]. On the other hand, less attention has been paid to the fatigue of welded tubular components made of high-strength steel material, especially for their low-cycle fatigue behaviour and design [16]. Valuable experimental data concerning the low-cycle fatigue performance of high-strength steel tubular welded connections were reported in a series of publications by Waalen and Berge [27], Boge *et* al. [28] and Hochman *et* al. [29]. T-joints, fabricated from seamless tubes with yield strength of 500MPa and chord diameter and thickness of 323.8mm and 15.9mm were tested under cyclic in-plane bending, out-of plane bending and axial loading, resulting in low-cycle fatigue failure between 3,000 and 200,000 loading cycles. The experimental results obtained from the three studies were compared with a large data-set and design provisions, and new $S-N$ curves were proposed for the low-cycle fatigue range corresponding to less than 10^5 load cycles. More recently, experimental data concerning welded tubular X-joints, with yield strength higher than 700MPa, under strong cyclic loading, were presented by Varelis *et* al. [30, 31]. The comparison of the experimental results with existing design provisions highlighted the conservative predictions of available design equations for the fatigue life of welded joints made of high-strength steel material within the low-cycle fatigue regime. It was also reported that for this low-cycle fatigue regime, a strain-based design methodology is more suitable to predict the experimental results, as opposed to the stress-based design approach extensively used in fatigue design.

The current work focuses on the ultra low-cycle fatigue performance of high-strength steel tubular welded X-joints. The specimens represent the X-brace joints of an offshore wind turbine jacket substructure considered for installation at a depth of 55m with a scaling factor of 1:3 employed in the JABACO project [6]. The X-joint specimens have been manufactured using S420 and S700 steel grade tubes and are subjected to extreme cyclic in-plane bending, leading to ultra low-cycle fatigue failure within less than 100 cycles. Furthermore, rigorous numerical models are used to simulate the experimental response of the specimens and examine whether finite element models can

provide accurate predictions for the bending moment-displacement global response and for local strains at critical locations. Comparison is also conducted between the present experimental data and relevant test results on mild or high-strength steel welded tubular components as well as design predictions from existing codes and standards.

The present paper is structured in the following manner. The experimental program and the testing results are described in detail in Section 2. Subsequently, the numerical model used for simulating the experiments is presented in Section 3 and comparisons with respect to the experimental data are provided. In Section 4, the experimental findings are compared with relevant experimental data reported in the literature and with predictions from existing code provisions. Finally, in Section 5, some important conclusions are summarised.

2. Experimental Program

The experimental program consists of seven ultra low-cycle fatigue tests on high-strength steel tubular welded X-joints. The tubular members used for fabricating the connection have been provided by SSAB, Stockholm, Sweden. The specimens have been fabricated in Hollandia Systems, Rotterdam, Netherlands according to the American Welding Society, Structural Welding Steel (AWS D1.1) [32] provisions for the tubular member welds and in accordance with appropriate Welding Procedure Specifications (WPSs) developed by the authors, in cooperation with Hollandia Systems, so that the specimen welds are representative of those found in offshore steel platforms.

2.1. Description of specimens

The seven X-joint specimens are denoted as $X_1 - X_7$. The first set of X-joints ($X_1 - X_4$) are fabricated using tubular components made of S420 steel grade with external diameter and thickness equal to 219.1mm and 10mm corresponding to a diameter-to-thickness ratio (D/t) of about 22. In addition, S700 tubes with external diameter and thickness of 273mm and 10mm and D/t equal to 27 are used for manufacturing specimens $X_5 - X_7$. For convenience, connections $X_1 - X_4$ and $X_5 - X_7$ will be grouped to

"Joint-1" and "Joint-2" assemblies. The three-dimensional configuration of the specimens is depicted in Fig. 1, while the geometric properties of each joint are summarised in Table 1. As shown in Fig. 1, the free ends of the tubular components are capped with welded plates for the requirements of testing. For clarity, the four chord crown locations where strain gauges are attached, are labeled as (1), (2), (3), (4), starting from the upper left corner and proceeding clockwise; the two crown locations located above the braces are labeled as (1), (2) and the other two crown points are represented by numbers (3) and (4). Strain measurements are also obtained at the point where the maximum principal strains/stress arise during the linear elastic analysis of Joint-1 and Joint-2 connections, subjected to monotonic/cyclic in-plane bending. This additional location is labeled in Fig. 1 as "in-between" point.

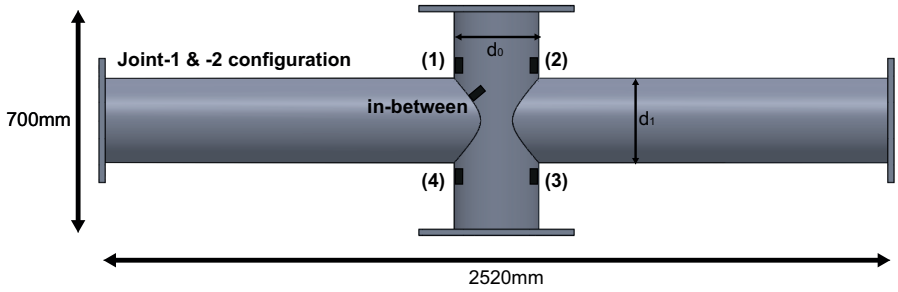

Figure 1: Three-dimensional configuration of Joint-1 and Joint-2.

Table 1: Geometric properties of specimens $X_1 - X_7$.

Joint:	Joint-1				Joint-2		
Specimen:	X_1	X_2	X_3	X_4	X_5	X_6	X_7
d_0=d_1 (mm)	219.1				273		
t_0=t_1 (mm)	10				10		
β=d_1/d_0	1.0				1.0		
τ=t_1/t_0	1.0				1.0		
γ=$d_0/2t_0$	10.96				13.65		

2.2. Material characterisation

A series of laboratory tests on strip specimens (coupons) extracted from the tubes of the same heat as those used for the fabrication of the specimens are performed to determine the monotonic and cyclic properties of the steel material in the inelastic range. The material tests have been performed using an Instron servo-hydraulic actuator of

250kN capacity. An anti-buckling device, shown in Fig. 2, is also used in the fully-reversed cyclic tests to restrict buckling of the specimens under compressive loading. The resulting stress-strain curves obtained from those coupons are presented in Fig. 3. Monotonic tests showed a 0.2% proof stress/ultimate strength of 519/585MPa and 745/840 MPa for the S420 and S700 steel grades respectively. Furthermore, cyclic tests at 2% strain amplitude indicated a minor cyclic hardening in both metals during initial load cycles. The welding materials are selected according to the WPSs developed for each joint configuration and their nominal grades overmatch the nominal yield strength of S420 and S700 steel grades by 29% and 6% respectively, which complies with the design provisions of DNVGL [33, 34] and is in accordance to common practice in offshore steel construction.

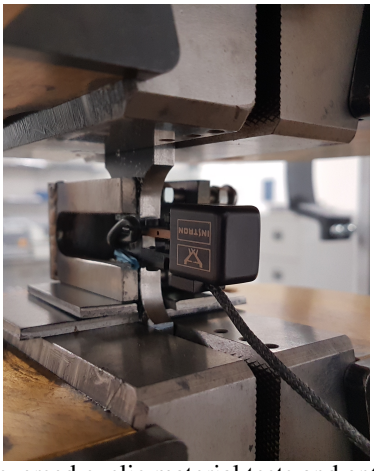

Figure 2: Fully-reversed cyclic material tests and anti-buckling device.

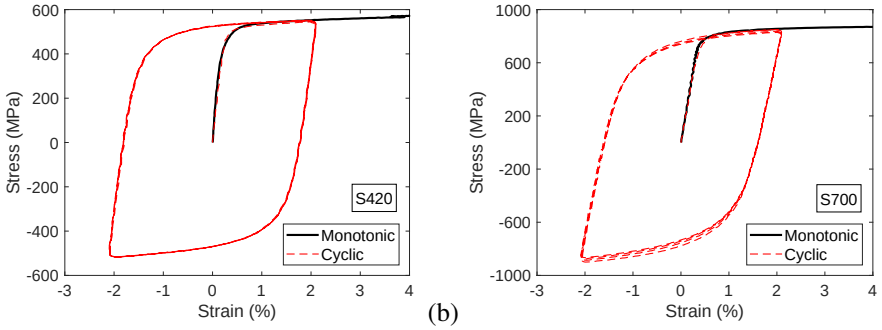

Figure 3: Monotonic and cyclic stress strain response obtained from testing coupon specimens extracted from tubes (a) S420 steel grade and (b) S700 steel grade.

2.3. Instrumentation

The specimens are properly instrumented during testing to record the force-displacement response and the induced strains at the locations of interest and to identify through-thickness cracking. The applied load is measured directly from the load cell of the actuator system and is recorded with the use of an external data logger. Displacement measurements are obtained with the use of string potentiometers, placed as shown in Fig. 4(a) in order to measure accurately the actual vertical displacement of the brace end. Local longitudinal strains are measured at crown locations of the chord with the use of uni-directional five-element-strip strain gauges (FXV-1), oriented perpendicular to the weld toe. Two FXV-1 series are used in every experiment, placed on chord crown points as shown in Fig. 4(b), at distance 5-9mm from the weld toe. In the majority of the tests, two additional strain gauges are attached at the "in-between" location of the chord side (Fig. 1), at distance of 5-25mm from the weld toe.

(a) 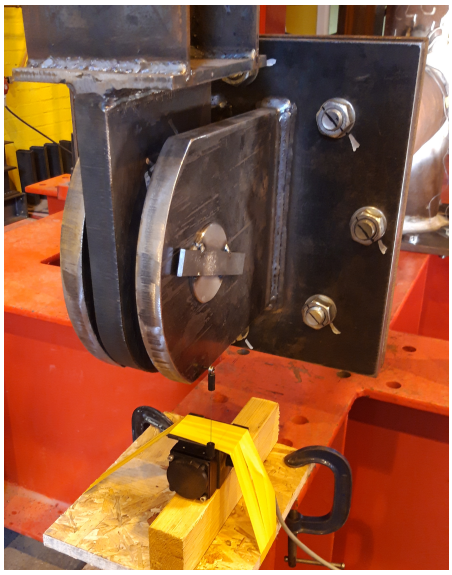 (b) 

Figure 4: (a) End brace displacement measurement and (b), local strain measurements in specimens X_1-X_7.

In the present test, initiation and propagation of surface cracks is monitored with a camera, shown in Fig. 5, while failure is defined as through-thickness cracking. To detect the stage at which the crack develops through the thickness of the tube wall,

a small hole has been drilled on the capping plate of each specimen, prior to testing, and two smoke flares are inserted into the chord; subsequently the hole is sealed with a re-usable envelope. As shown in Fig. 5, when the through-thickness crack occurs, the trapped smoke escapes through the crack so that it is visible, and the corresponding number of cycles to failure is recorded.

Figure 5: Trapped smoke escaping through the crack which allows the measuring of the number of cycles to failure.

2.4. Experimental set-up

The experiments are conducted at the Structures Laboratory of The University of Edinburgh (School of Engineering) using an Instron 8800 servo-hydraulic actuator system of 1MN capacity. The three-dimensional configuration of the experimental set-up is presented in the sketch of Fig. 6 and the main parts of the set-up are denoted in that figure. For clarity, a close-up sketch of the connection between the specimen and the experimental set-up is illustrated in Fig. 7, while a photo of the constructed set-up is depicted in Fig. 8 for the sake of completeness. The hydraulic actuator is mounted on the test-ring to assemble a self-reacting structural system. The actuator is placed vertically, hanged from the horizontal crossbeam. The other end of the actuator is pin-connected at the center of the 3.3m-long spreader beam, as shown in Figs. 6 and 7 initially located at a distance of 200mm from the top of the specimen. A pin-ended

column, highlighted in Fig. 6, connects the spreader beam with the specimen, allowing for axial deformations to take place while preventing the development of axial tensile forces (stretching) on the bracings. The X-joint specimen, shown more clearly in Fig. 7, is rigidly supported at the base of the chord member, while the top edge of the chord is capped with a welded plate to preserve symmetry. Two lateral support systems are fixed on the test-rig to ensure the safe operation of the actuator by restricting sideways movements of the crossbeam, which is free to move in the vertical direction. During testing, the actuator moves vertically together with the spreader beam, which imposes a repeated displacement of alternating sign at the ends of the braces, introducing in-plane cyclic bending loading at the welded connection. The experimental arrangement is symmetric and the lateral distance between the centroid of the chord and the load application points is equal to 1.5m. The experiments are conducted under a displacement-control scheme with ratio R=-1 (fully-reversed displacement) and the movement of the hydraulic actuator is controlled via the Instron WaveMatrix software.

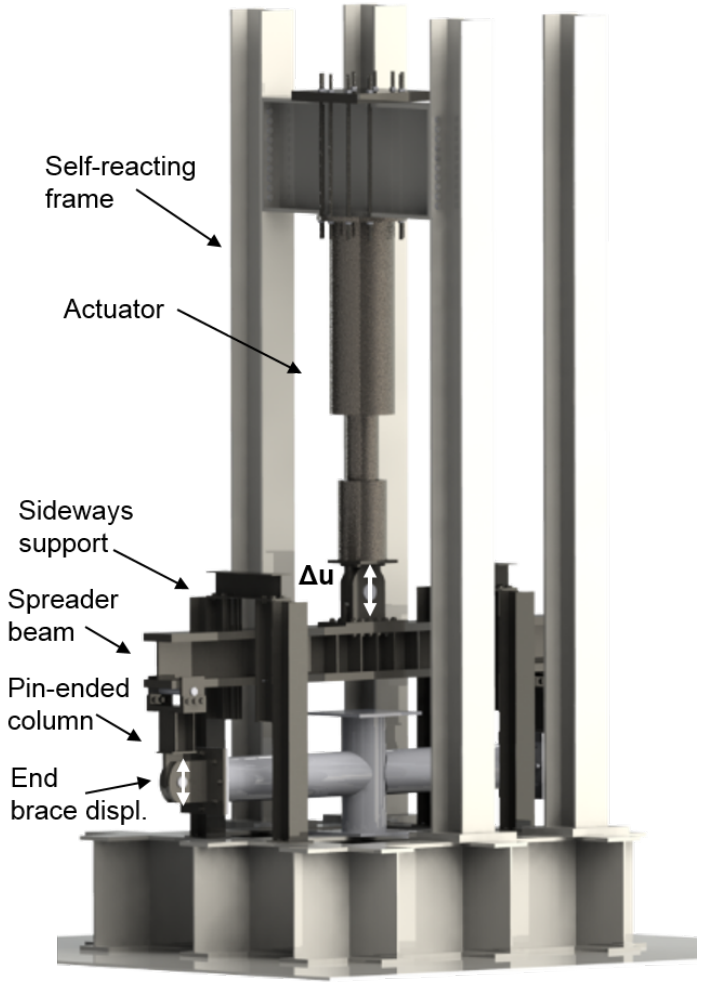

Figure 6: Three-dimensional computer visualisation of experimental set-up.

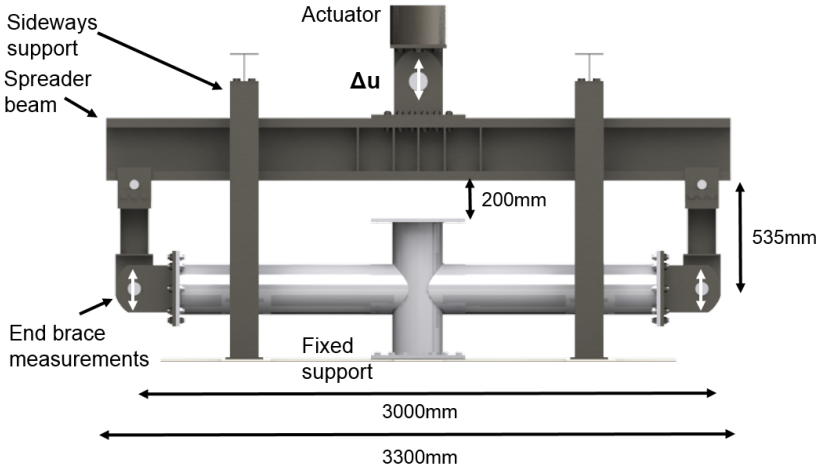

Figure 7: Schematic representation of in-plane cyclic bending testing arrangement.

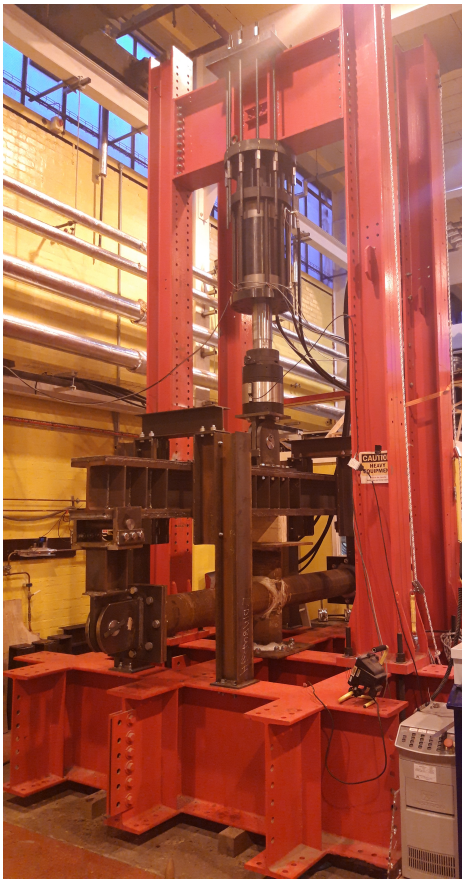

Figure 8: Photo of the experimental set-up.

Each tubular X-joint specimen is subjected to a specific displacement amplitude, in order to explore the ultra low-cycle fatigue performance of the welded tubular steel joints at a wider range of fatigue life. A preliminary finite element analysis is conducted prior to the experiments to support the selection of the testing displacement amplitudes, shown in Table 2 together with the value of the maximum applied moment normalised with respect to the "yield bending moment" M_y. The value of M_y is defined as the bending moment that corresponds to first yielding of the joint, computed numerically through the finite element model under monotonic loading conditions. The M_y values are equal to 109kNm and 239kNm for Joint-1 1 and Joint-2, respectively. The resisting bending moment decreases gradually over the loading cycles due to material degradation.

Table 2: Testing conditions of specimens $X_1 - X_7$.

Joint:	Joint-1				Joint-2		
Specimen:	X_1	X_2	X_3	X_4	X_5	X_6	X_7
Edge brace displ. (mm):	± 29	± 35	± 41	± 47.5	± 31.6	± 38	± 48
$\lvert M_{max}/M_y \rvert$	1.19	1.34	1.40	1.49	1.16	1.32	1.51

2.5. Experimental results

The bending moment-displacement response recorded at various load cycles during testing of specimens X_1-X_4 and X_5-X_7 is presented in Fig. 9 (a-d) and Fig. 10 (a-c), respectively. Figs. 9 and 10 show that all specimens experience a small amount of cyclic hardening during the first load cycle, while the hysteresis response changes slightly prior to damage initiation, in which case, the resisting moment capacity starts decreasing noticeably. The sudden decrease observed in the bending moment-displacement diagram of specimen X_6 during the initial load cycles (Fig. 10(b)) is attributed on a loose bolted connection and not to any material damage. In this case, the test was interrupted to tighten the bolts in this joint, and the slippage effects have been eliminated.

In Joint-1 specimens and in particular specimen X_2, which is subjected to brace edge displacements of $\pm$35mm, strength reduction due to material degradation initiates at

about the 10^{th} load cycle, whereas damage effects become more pronounced after 30 load cycles. Through-thickness cracking occurred at the 47^{th} load cycle and the test is interrupted after 49 cycles, where the maximum resisting bending moment has been reduced by 42% with respect to the corresponding maximum bending moment of the first cycle. In specimen X_5 of the Joint-2 group, through-thickness cracking occurs at the 58^{th} load cycle. In this case, material degradation initiates after 15 load cycles and becomes noticeable after 40 load cycles. The experiment is interrupted after 65 cycles, where the structural capacity has been reduced by almost 30%.

The experimental results show that in both joint configurations, strength degradation manifests initially at low rate, while rapid reduction of resisting bending moment is observed as the specimen approaches failure, indicating two distinct stages of damage evolution.

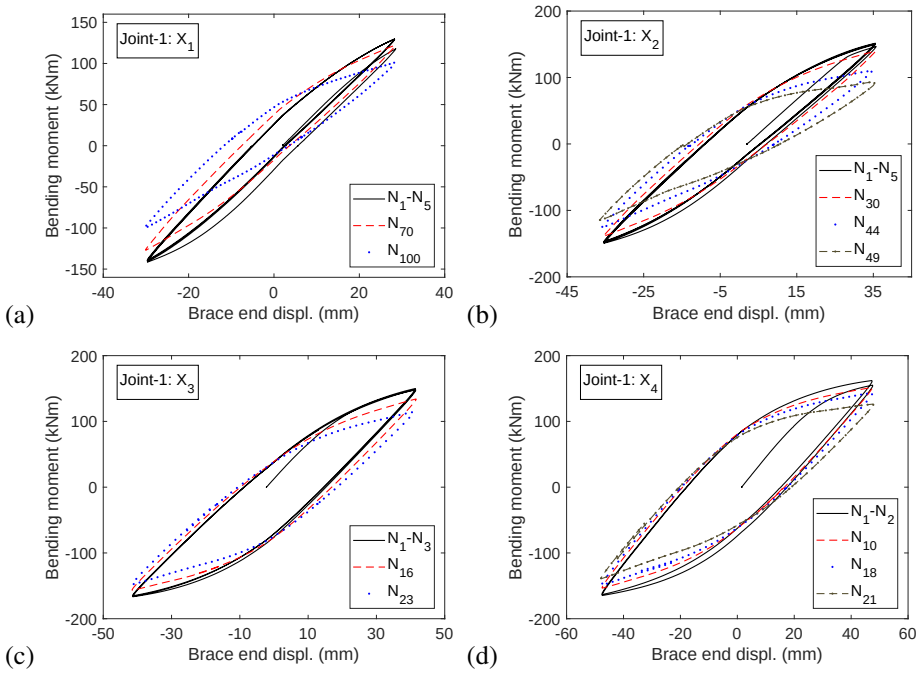

Figure 9: Bending moment-displacement response obtained from specimens X_1-X_4.

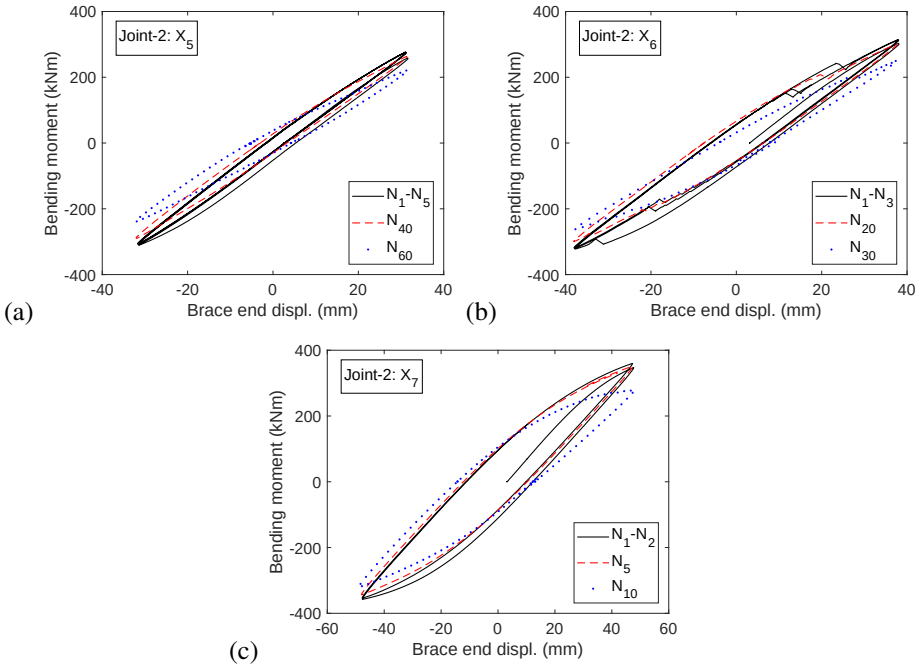

Figure 10: Bending moment-displacement response obtained from specimens X_5-X_7.

Local strains are measured at the chord member at the two crown locations and results are presented in Fig. 11 for Joint-1 and Joint-2 specimens. The distance of each strain gauge from the weld toe is denoted at the legend of each figure, while the chord crown location where measurement is obtained, is defined using the number in parenthesis. Strain gauges have also been attached at the "in-between" location, shown in Fig. 1, and strain measurements have been obtained, but the recordings are significantly lower than the strains obtained at the chord crown locations.

Strain measurements are analysed in terms of strain-range evolution with respect to loading cycles. Fig. 11, shows that the induced strain-range due to cyclic loading increases slightly during initial load cycles, reaches a constant value and subsequently, it starts decreasing when cracks are formed at the weld toe. Clearly, after a substantial number of load cycles, significant surface cracking starts developing and becoming quite visible, and the corresponding strain recordings start decreasing rapidly.

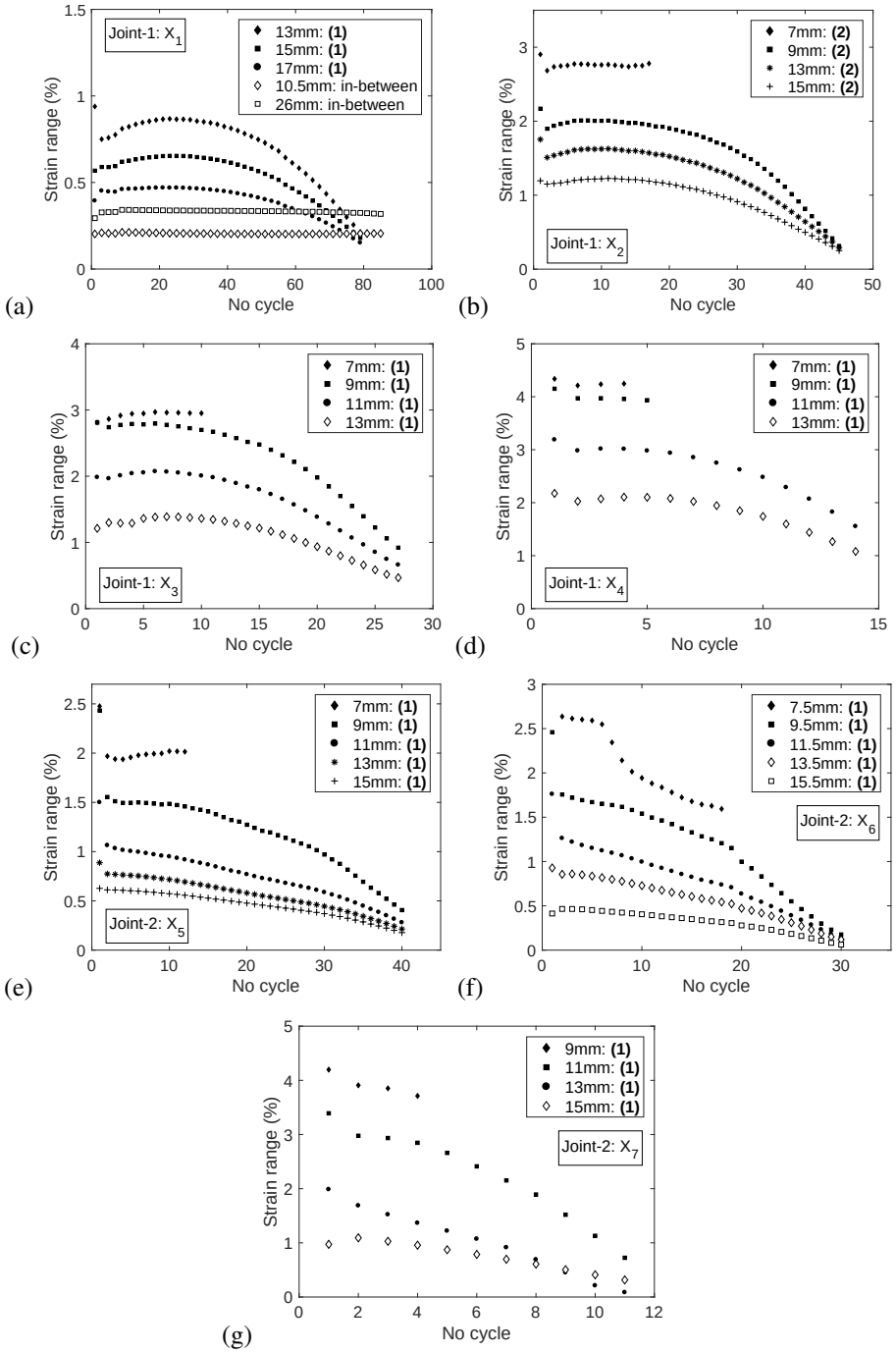

Figure 11: Strain range evolution over the loading cycles obtained from testing specimens X_1-X_7.

The final fractured shapes of specimens X_1-X_7 are illustrated in Fig. 12, while the fatigue crack initiation stage of an example case (specimen X_6) is presented in Fig. 13. In all cases, through-thickness crack initiated at one of the four chord crown locations. Continuation of cyclic loading resulted in propagation of initial cracks along the weld toe in a pattern which is symmetric with respect to the crown location.

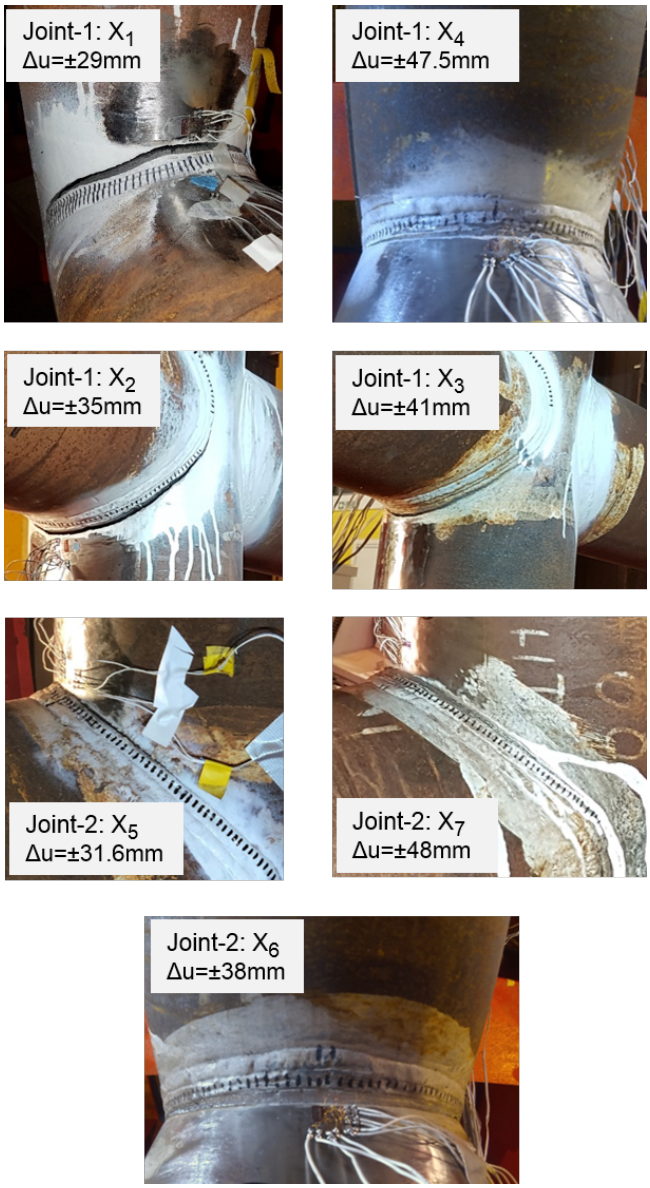

Figure 12: Failed specimens X_1-X_7

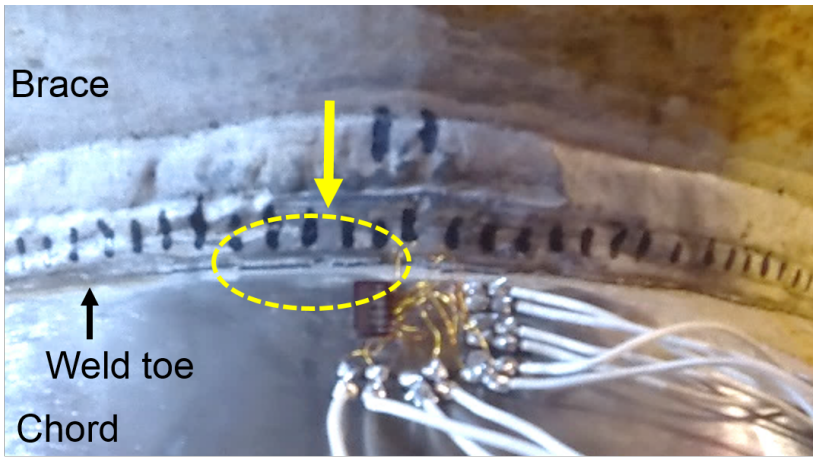

Figure 13: Fatigue crack at early stage of test X_6.

3. Numerical Simulation and Comparison with Test Data

3.1. Finite element model

The experimental results of the present study are numerically simulated with advanced finite element models. Both Joint-1 and Joint-2 are modeled with the use of commercial finite element package ABAQUS/Standard [35]. The main features of the finite element model, used to simulate the mechanical response of Joint-1 and Joint-2 specimens, are presented in Fig. 14. The finite element mesh at chord-brace intersecting area of the models of Joint-1 and Joint-2 is shown in Fig. 15. Double symmetry is considered for computational efficiency with the appropriate boundary conditions and therefore, only 1/4 of the X-joint specimen is modeled. Two reference points are also imposed to simulate the boundary conditions applied during testing. Reference point RP-1 is kinematically coupled with the end of the brace, to simulate the hinge in the experimental set-up shown clearly in Fig. 7, given the fact that the end of the brace is capped. Point RP-1 is unrestrained in the axial direction of the brace, while the vertical displacement is prescribed in the analysis and corresponds to the brace edge displacement recorded during testing. Additionally, reference point RP-2 is kinematically coupled with the end nodes at the top section of the chord, simulating the cap welded plate. Furthermore, the nodes at the bottom edge of the chord member are fully fixed, as in the experiment.

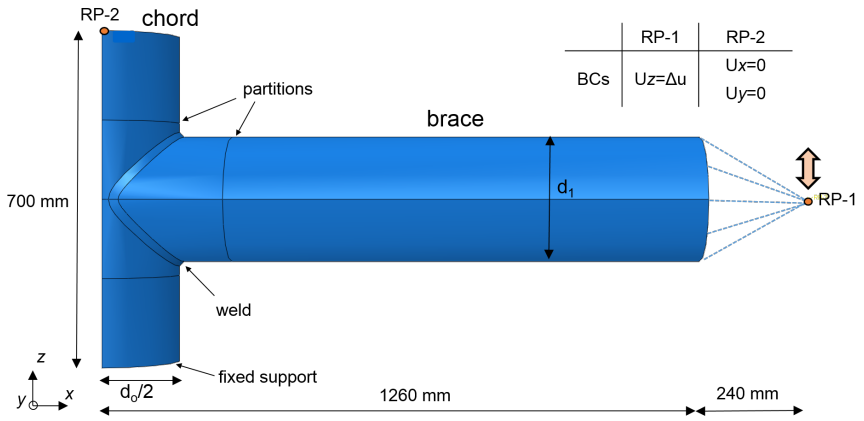

Figure 14: Numerical model of the test specimen.

The finite element models of Joint-1 and Joint-2 are meshed with linear solid finite elements (C3D8) and include the accurate modeling of the weld geometry based on the provisions of the American Structural Welding Code AWS D1.1 [32]. A sensitivity analysis has been conducted, showing that 43000 and 48000 linear solid finite elements are adequate for discretising Joint-1 and Joint-2 configurations. Joint-1 model uses 60 elements along the circumference of the brace and 28 elements around the circumference of the chord, while 5 elements are considered through the thickness of the brace and the chord to provide a well-posed mesh at the welding area. Similarly, in Joint-2 model 64 elements are adequate for discretising the circumference of the brace and 32 for the chord, while 5 elements are used through the thickness of each part. In the longitudinal direction the "single bias meshing" technique is used, leading to finer discretisation close to the brace-chord intersection and coarser mesh away from the weld, where the stresses and the strains are significantly lower.

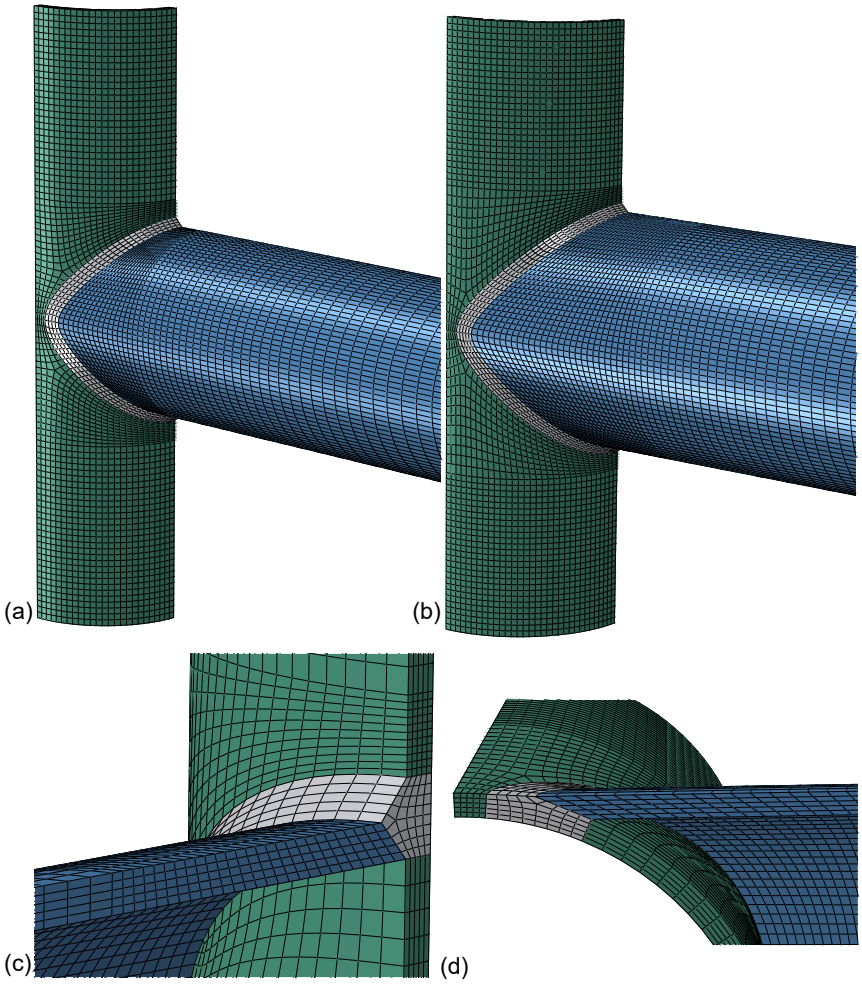

Figure 15: Discretised finite element model of (a) Joint-1 and (b) Joint-2. Detail representation of the welded area of Joint-2 at (c) the crown point and (d), the saddle point.

3.2. Constitutive model

The use of an appropriate cyclic-plasticity model is of great importance for simulating accurately the inelastic response of the specimen. The constitutive model employed herein is based on a J_2 (von Mises) cyclic elasto-plasticity model with mixed hardening. The numerical implementation of the material model is utilised through the use of an external material user subroutine (UMAT), developed by the authors and presented elsewhere [36]. The governing equations of kinematic and isotropic hardening rules employed are presented in Eqs. (1-2) below. Kinematic hardening obeys the Chaboche [37] model, with four nonlinear backstress tensors, as proposed in [38, 39]

$$\dot{\boldsymbol{\alpha}} = \sum_{i=1}^{4} (C_i)\, \dot{\boldsymbol{\varepsilon}}^p - \sum_{i=1}^{4} \left(\gamma_i \boldsymbol{\alpha}^i\right) q \tag{1}$$

whereas isotropic hardening is represented with the use of an exponential function.

$$k(q) = \sigma_y + Q_\infty \left(1 - e^{-bq}\right) \tag{2}$$

Eq. (1), expresses the rate of the backstress tensor $\dot{\boldsymbol{\alpha}}$, which consists of four nonlinear backstresses ($\boldsymbol{\alpha}^i$), $\dot{\boldsymbol{\varepsilon}}^p$ is the rate of the plastic strain tensor and q is the equivalent plastic strain. Furthermore, in Eq. (2), k defines the size of the yield surface, σ_y is the initial yield stress, while $C_i, \gamma_i, Q_\infty, b$ are additional material parameters. All material parameters of the constitutive model are calibrated for each steel grade separately, so that the small-scale tests on strip specimens, shown in Fig. 3, are accurately represented. The material parameter sets adopted in the present analysis for S420 and S700 steel grades are listed in Table 3.

Table 3: Material properties of constitutive model.

Mat.	E (MPa)	v	σ_y (MPa)	Q_∞ (MPa)	b	C_{1-4} (MPa)	γ_{1-4}
S420	$1.9{\cdot}10^5$	0.3	425	-50	100	20,000	610
						8,000	420
						3330	220
						1,667	30
S700	$1.9{\cdot}10^5$	0.3	650	-60	100	23,330	500
						11,330	240
						8,000	180
						550	20

The finite element models shown in Figs. (14-15) are employed for the numerical simulation of the experimental procedure for specimens X_1 to X_7. The numerical analyses are conducted considering the actual displacement amplitudes recorded at the brace end during testing and listed in Table 2. Comparisons between numerical and experimental results are provided in detail for the two most extreme cases, involving specimens X_4 and X_7, and more briefly for the other experiments. It should be underlined that the numerical simulation refers to the first 5-10 load cycles, corresponding to the first stage of the welded joint response. In the subsequent stages, the joint material undergoes degradation and a cyclic plasticity model may not be adequate to describe the actual material behaviour. In such a case, coupled plasticity-damage models are required to simulate the mechanical response of the steel material, but such a modeling effort lays outside the scope of the present study.

Fig. 16 presents the bending moment-displacement diagram obtained from the numerical analysis and experimental testing of specimens X_4 and X_7. The comparison shows the ability of the finite element model to simulate accurately the inelastic bending moment-displacement response of the X-joint specimens under consideration. Comparisons are also provided in terms of strain-range predictions ($\Delta\varepsilon$) obtained at location (1) and the corresponding results are presented in Fig. 17. The results obtained from the finite element model are presented with a dashed line. The strain gauges located very close to the weld toe failed during the initial load cycle in both tests probably because of the high value of strain developed at that location and, therefore, measurements are provided for the other four strain gauges located at distances ranging from 7mm to

15mm away from the weld toe. Fig. 17 shows that the numerical model predicts the experimental values of strain range satisfactorily for both joints. Furthermore, the distribution of von Mises stress obtained from the numerical simulation of specimens X_4 and X_7 is depicted in Fig. 18, corresponding to the maximum bending moment, and shows the most highly stressed areas in each specimen.

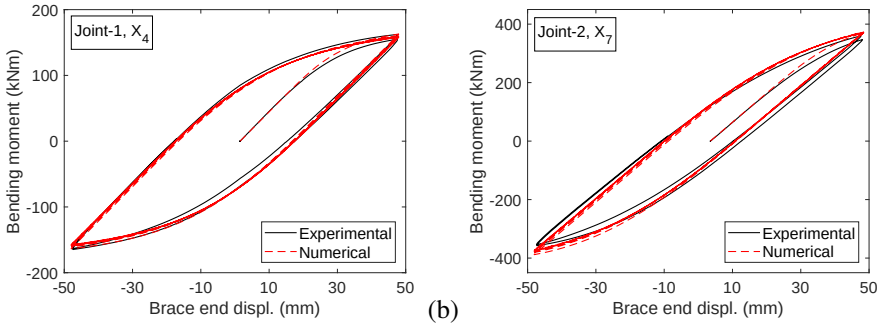

Figure 16: Bending moment-displacement relation obtained through numerical simulations and experimental testing of specimens (a) X_4 and (b) X_7.

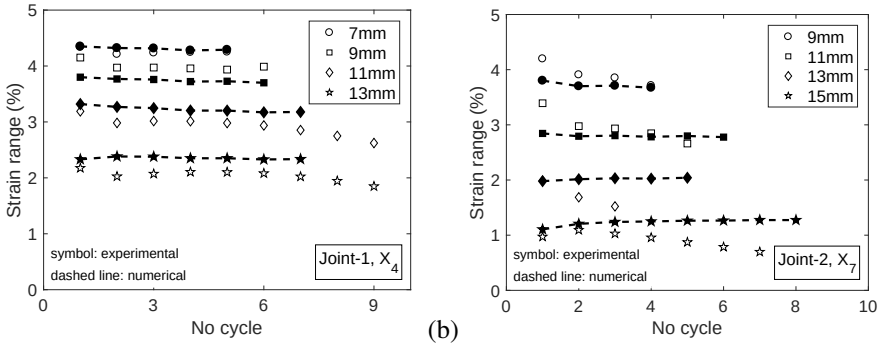

Figure 17: Strain range evolution obtained at location (1) through numerical analysis and experimental testing of specimens (a) X_4 and (b) X_7.

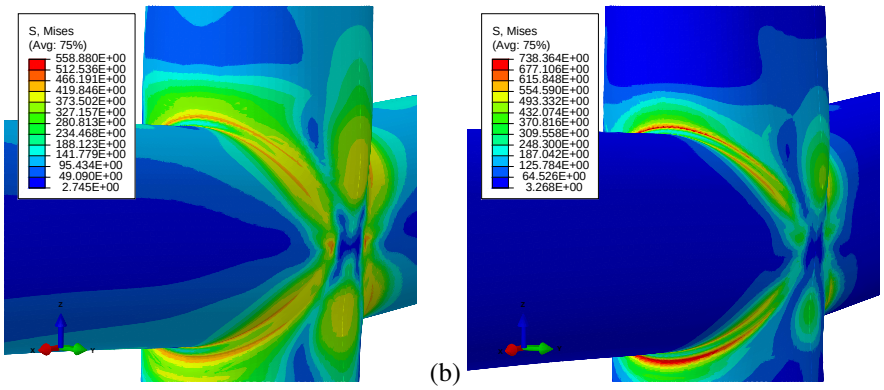

(a) (b)

Figure 18: Von Mises stress distribution obtained from the simulation of specimens (a) X_4 and (b) X_7 at the moment of maximum bending moment.

4. Comparison with design provisions and relevant available data

4.1. Evaluation of hot-spot stress/strain range

Experimental and numerical results are further analysed by correlating the so-called "hot-spot strain" range ($\Delta\varepsilon_{hs}$) and "hot-spot stress" range ($\Delta\sigma_{hs}$) with the number of cycles to failure (N_f). Herein, $\Delta\varepsilon_{hs}$ is computed by extrapolating linearly the local strain range values obtained from either numerical results or experimental data at the location of the weld toe. It is noted that the extrapolated value $\Delta\varepsilon_{exp,hs}$, obtained from the experimental results, is calculated using the measurements recorded after the first two load cycles to ensure that the induced strain range has reached a constant value (see Fig. 11).

The hot-spot strain range values of specimens $X_1 - X_7$ obtained using test data ($\Delta\varepsilon_{exp,hs}$) and the numerical results ($\Delta\varepsilon_{FEM,hs}$) are presented in Table 4 along with the number of cycles to through-thickness cracking (N_f) as measured in the experiments. In specimen X_1, a single value is presented as the second FXV-1 series has been attached on the brace crown location and the recordings are significantly low ($\Delta\varepsilon_{exp,hs}$=0.5%). Two hot-spot strain range values are computed in each experiment and in the majority of cases differ slightly with respect to each other. A significant difference of measurement at each side of the specimen is observed only in test X_5. Post-processing of the experimental data showed that, in this test, the induced displacement range has been

slightly unsymmetrical, and this is attributed to geometric imperfections in the specimen, leading to higher strain values on the weld of one side of the chord with respect to the other weld. Furthermore, comparison of the experimental data with the numerical results shows that the finite element model predicts very accurately the measured hot-spot strain range.

Hot-spot stress range values ($\Delta\sigma_{hs}$) are also evaluated for each experiment following the provisions of CIDECT (Committee for International Development and Education on Construction of Tubular Structures) [40]. The nominal stress range ($\Delta\sigma_{nom}$) at the braces due to bending is calculated considering the applied bending moment and the elastic modulus of the pipe, while the stress concentration factors (SCFs) of Joint-1 and Joint-2 connections are obtained: (a) using the parametric equations proposed in CIDECT [40], and (b) using the finite element models described in Section 3. In the latter case, a small load has been applied so that plastic deformation is eliminated in the calculation of the SCF value. The resulting SCFs values are presented in Table 4, highlighting that the numerically computed SCFs are very similar with those calculated using the parametric formulas in CIDECT [40]. The hot-spot stress range values ($\Delta\sigma_{hs}$) presented in Table 4 is calculated by multiplying the SCF value with the nominal stress range value $\Delta\sigma_{nom}$. In this calculation, the highest of the two SCF values obtained for each type of connection is used. It should be noted that the $\Delta\sigma_{hs}$ are very high, much higher than the yield stress of the material, therefore these stress values should be considered as "pseudo-elastic" stresses.

Table 4: Main testing results of specimens $X_1 - X_7$.

Specimen	N_f	$\Delta\varepsilon_{exp,hs}$ (%)		$\Delta\varepsilon_{FEM,hs}$ (%)	SCF		$\Delta\sigma_{hs}$ (MPa)
					CIDECT	FEM	
X_1	88 **(1)**	1.72 **(1)**	**(-)**	1.71 **(1 & 2)**			2797
X_2	47 **(3)**	3.65 **(2)**	3.82 **(3)**	3.82 **(1 & 2)**	3.119	3.386	3052
X_3	21 **(4)**	5.97 **(1)**	5.83 **(2)**	5.63 **(1 & 2)**			3240
X_4	15 **(1)**	7.07 **(1)**	7.09 **(2)**	6.66 **(1 & 2)**			3371
X_5	58 **(1)**	3.63 **(1)**	3.04 **(2)**	3.06 **(1 & 2)**			3750
X_6	34 **(1)**	4.43 **(1)**	4.28 **(2)**	4.17 **(1 & 2)**	3.347	3.223	4067
X_7	10 **(2)**	8.05 **(1)**	8.28 **(2)**	6.92 **(1 & 2)**			4583

Note: The number within $(\cdot)$ indicates the reference location.

4.2. Comparison with relevant test data and stress-based provisions

The design of tubular welded joints under ultra low-cycle fatigue remains a challenging task, as limited guidance is available in relevant design codes and standards, especially for high-strength steel material. The methodologies proposed in DNVGL-RP-C203 [33], CIDECT [40], API RP2A [41] and EN 1993-1-9 [42] for the fatigue design of welded tubular connections have been developed for regular steel material and are valid for cases mainly associated with high-cycle fatigue; i.e. with fatigue failure at a number of cycles that exceeds $N_f \geq 10^4$. Nevertheless, in the absence of design guidance for low-cycle fatigue, it has been proposed in Appendix F.1 of DNVGL-RP-C203 [33] to extrapolate the proposed $S-N$ curves into the low-cycle fatigue regime. In the present study this extrapolation is performed and those design provisions are compared with respect to experimental results obtained from low-cycle fatigue tests. In addition to the present experimental results, experimental data reported in the literature are also plotted together with the design $S-N$ curves provided in [33, 41] as well as the $S-N$ curve proposed by Hochman *et* al. [29], for predicting the fatigue life in the range of $1 \leq N_f \leq 10^3$. The $S-N$ curves proposed in CIDECT [40] and EN 1993-1-9 [42] are not included in the plot, because, for the range under examination, they are almost identical with the curve proposed in DNVGL-RP-C203 [33].

The experimental results obtained from specimens $X_1 - X_7$ and those reported in previous works [19, 27, 28, 29, 31] are plotted in Fig. 19 in terms of the hot-spot stress

range ($\Delta\sigma_{hs}$) and number of cycles to failure (N_f). The examined data are collected from large-scale tests on tubular welded components fabricated from mild steel or high-strength steel metal alloys. Fig. 19 shows that the results of the present investigation fall well beneath the $S-N$ curve proposed in DNVGL-RP-C203 [33] while the predictions of this code in particular are satisfactory for tests with $N_f \geq 10^2$. On the other hand, the $S-N$ curve proposed in API RP2A [41] is quite conservative and will not be discussed further. In the log$\Delta\sigma_{hs}$-logN_f plot, the results obtained from specimens $X_1 - X_7$ show very small slope of the corresponding fatigue curve, indicating that the hot-spot stress methodology employed in the present work may not be a reliable measure of fatigue resistance in the ultra low-cycle fatigue regime. It should be considered that under intense cyclic loading, the structural components are loaded far beyond their elastic limit and the bending moment-displacement relation is highly nonlinear. Hence, the hot-spot stress concept, which is mainly based on the concept of elastic stress concentration, might not be reliable for describing the behaviour of tubular welded structural components in the range of ultra low-cycle fatigue ($1 \leq N_f \leq 10^2$) and predicting the fatigue life.

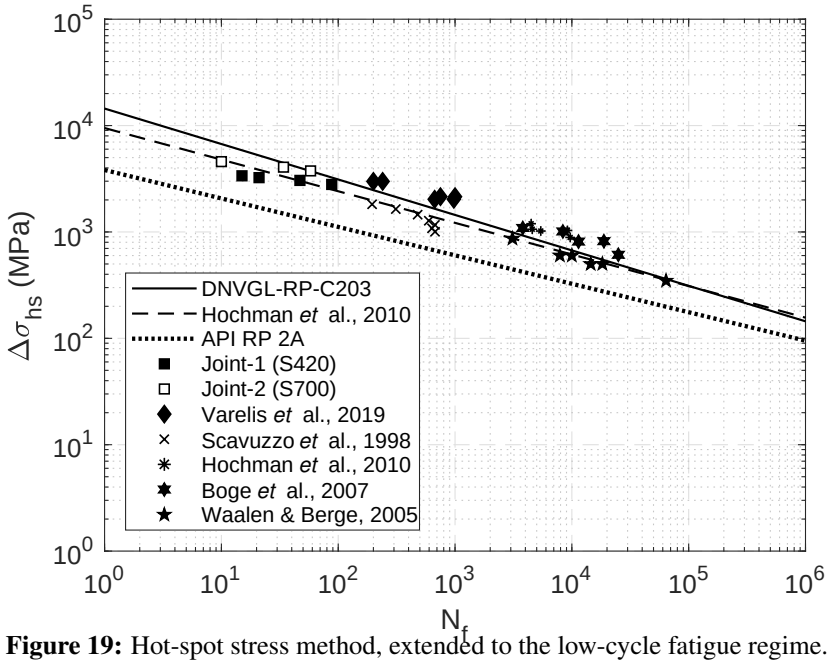

Figure 19: Hot-spot stress method, extended to the low-cycle fatigue regime.

4.3. Comparison with relevant data and codes using a strain-based framework

A different approach is adopted in DNGVL-RP-C208 [34] standard provisions. DNVGL-RP-C208 [34] proposes a design methodology against ultra low-cycle fatigue using the hot-spot strain range ($\Delta\varepsilon_{hs}$) and a modified Coffin-Manson equation [43, 44]. For tubular welded connections, a mean and a design $\Delta\varepsilon_{hs}$-N_f curve are presented in Section 7.12 of DNVGL-RP-C208 [34]. The mean curve is derived based on the limited available experimental data reported in the literature. The design $\Delta\varepsilon_{hs}$-N_f curve is constructed by substracting three standard deviations of 0.2 in the logN scale.

The experimental findings of the present study as well as those reported in [18, 19, 31] are analysed in terms of hot-spot strain range ($\Delta\varepsilon_{hs}$) against number of cycles to failure (N_f) and the results are presented in Fig. 20. Comparing the present experimental data with those reported by Skallerud *et* al. [18] concerning steel T-joints with yield strength of 360MPa, it is deduced that high-strength steel tubular joints perform equally well with mild steel connections under intense cyclic loading.

The experimental data ($\Delta\varepsilon_{exp,hs} - N_f$) are also compared with respect to the mean $\Delta\varepsilon_{hs}$-N_f curve and the design $\Delta\varepsilon_{hs}$-N_f curve provided in DNGVL-RP-C208 [34]. The mean curve proposed in DNGVL-RP-C208 [34] is in very good agreement with the experimental results reported in the present study and those of Skallerud *et* al. [18]. The results of Varelis *et* al. [31] fall between the mean curve and the design curve. A possible explanation of this is that the tests in [31] were conducted under a load-controlled pattern with a load ratio of R=0.1, whereas the present experimental data and those reported by Skallerud *et* al. [18] are obtained using a displacement-control testing protocol with ratio of R=-1 (fully-reversed). The design $\Delta\varepsilon_{hs}$-N_f curve may underestimate the fatigue life of the tests with a number of cycles to failure less than 100, but provides satisfactory predictions with respect to the findings of Scavuzzo *et* al. [19]and Varelis *et* al. [31]. Comparing Fig. 19 with Fig. 20, it is concluded that the design of welded joints against ultra low-cycle fatigue should be preferably conducted in a strain-based framework, using an appropriate $\Delta\varepsilon_{hs}$-N_f curve. The methodology provided in DNVGL-RP-C208 [34] constitutes a basis for such an approach but additional

experimental data are required for validating the methodology and predict the ULCF life with good accuracy.

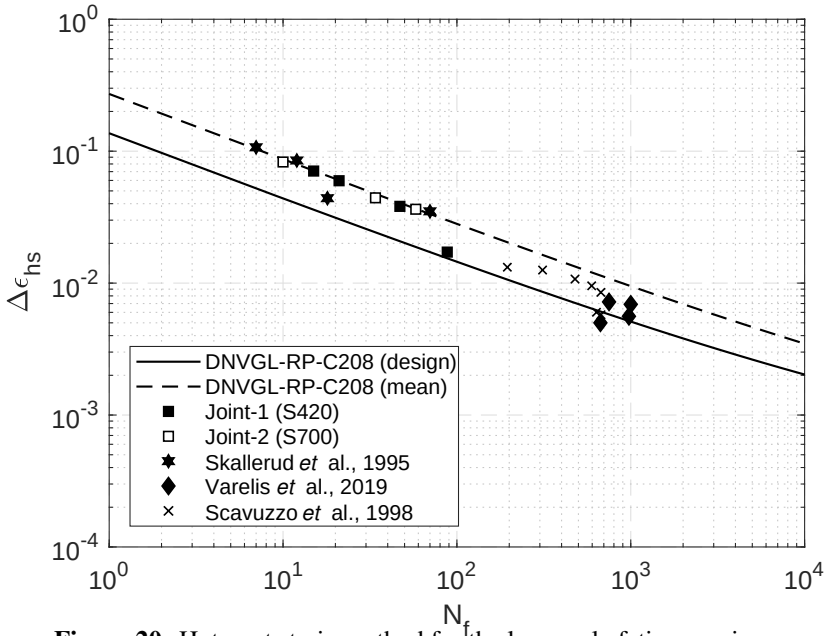

Figure 20: Hot-spot strain method for the low-cycle fatigue regime.

5. Conclusions

The present work investigates the fatigue performance of tubular welded X-joints, made of S420 and S700 steel material under severe cyclic loading conditions, using large-scale experiments and numerical simulations. The work refers to extreme loading exerted on representative tubular X-joints of an offshore wind structural system designed for installation in water depth of 55m, which may lead to low-cycle fatigue. Seven large-scale specimens are tested under intense cyclic in-plane bending, leading to failure with a number of cycles less than 100, which is referred to as "ultra low-cycle fatigue". Experimental results are provided in terms of bending moment-displacement relation, local strain measurements and the number of cycles to failure, which is defined as the stage where through-thickness crack occurs. The experimental program is simulated using rigorous finite element models, which employ advanced cyclic-plasticity models through in-house material subroutines. Very good comparisons are obtained in

terms of bending moment-displacement relation and local strain predictions.

The main purpose of the current experimental program is to provide additional information regarding the ultra low-cycle fatigue performance of steel tubular welded connections made of S420 and S700 steel, as very limited guidance is available in relevant codes and standards, especially for high-strength steel. The specimens from both steel grades provided similar structural fatigue behaviour whereas comparison with relevant data reported in the literature showed that under severe cyclic loading, high-strength steel welded connections perform equally well with mild steel welded connections. Therefore, the present results are quite promising for the use of high-strength steel in offshore applications.

In the last part of the paper, existing design provisions are validated against a large set of experimental data collected from the literature including also the present experimental results. The analysis results showed that the "hot-spot stress" method, extrapolated in the low-cycle fatigue regime, could be used for cases where failure is expected in more than 100 load cycles, but it might not provide accurate fatigue life predictions in the range of ultra low cycle fatigue, corresponding to less than 100 cycles. On the other hand, the strain-based method proposed in DNVGL-RP-C208 [34] provided fatigue life predictions of reasonable accuracy with respect to the experimental data. The present results can be employed for establishing a unified design methodology suitable for low-cycle fatigue of welded tubular connections ($1 \leq N_f \leq 10^4$), including the use of high-strength steel material, towards reducing the construction cost of offshore platforms and increasing their life-cycle performance.

Acknowledgement

The authors would like to thank the School of Engineering, The University of Edinburgh, Scotland, UK for supporting this research project through a PhD fellowship to the first author. Furthermore, the authors would like to thank Mr. Mark Partington and Mr. James Brennan from University of Edinburgh, Scotland, UK for their assistance in performing the experiments. The contribution of SSAB, Stockholm, Sweden for

providing the tubes of the connection and Hollandia Systems, Rotterdam, Netherlands for fabricating the specimens are greatly acknowledged. The authors would also like to thank Dr. Anna Zervaki, University of Thessaly, Volos, Greece, for her assistance in developing the WPS for manufacturing the specimens.

References

[1] H. Jeffrey, J. Sedgwick, ORECCA. European offshore renewable energy roadmap, Tech. rep., The University of Edinburgh (2011).

[2] J. Moccia, A. Arapogianni, J. Wilkes, C. Kjaer, R. Gruet, PurePower. Wind energy targets for 2020 and 2030, Tech. rep., European Wind Energy Association (EWEA) (2011).

[3] F. Selot, D. Fraile, G. Brindley, Offshore wind in Europe - Key trends and statistics 2018, Tech. rep., European Wind Energy Association (EWEA) (2019).

[4] Beatrice windfarm Ltd. https://www.beatricewind.com (2018).

[5] Alpha ventus windfarm park. https://www.alpha-ventus.de/ueberblick/ (2013).

[6] Rina, Development of modular steel jacket for offshore windfarms (JABACO), Tech. rep. (2019).

[7] W. Dong, T. Moan, Z. Gao, Long-term fatigue analysis of multi-planar tubular joints for jacket-type offshore wind turbine in time domain, Engineering Structures 33 (6) (2011) 2002–2014. doi:10.1016/J.ENGSTRUCT.2011.02.037.
URL https://www.sciencedirect.com/science/article/pii/S0141029611001088

[8] W. Dong, T. Moan, Z. Gao, Fatigue reliability analysis of the jacket support structure for offshore wind turbine considering the effect of corrosion and inspection, Reliability Engineering & System Safety 106 (2012) 11–27. doi:10.1016/J.RESS.2012.06.011.

[9] S. F. Mohammadi, N. S. Galgoul, U. Starossek, P. M. Videiro, An efficient time domain fatigue analysis and its comparison to spectral fatigue assessment for an offshore jacket structure, Marine Structures 49 (2016) 97–115. doi:10.1016/J.MARSTRUC.2016.05.003.
URL https://www.sciencedirect.com/science/article/pii/S0951833916300648

[10] Y. Bai, W.-L. Jin, Fatigue Reliability, Marine Structural Design (2016) 671–687.
URL https://www.sciencedirect.com/science/article/pii/B9780080999975000368

[11] B. Skallerud, On the relationship between low cycle fatigue and crack growth rate properties in welded steel components, Fatigue & Fracture of Engineering Materials & Structures 15 (1992) 43–56. doi:doi:10.1111/j.1460-2695.1992.tb00015.x.

[12] K. Nip, L. Gardner, C. Davies, A. Elghazouli, Extremely low cycle fatigue tests on structural carbon steel and stainless steel, Journal of Constructional Steel Research 66 (1) (2010) 96–110. doi:10.1016/J.JCSR.2009.08.004.

[13] J. Weigand, J. Berman, Behavior of butt-welds and treatments using low-carbon steel under cyclic inelastic strains, Journal of Constructional Steel Research 75 (2012) 45–54. doi:10.1016/J.JCSR.2012.03.007.

[14] P. Dong, X. Pei, S. Xing, M. Kim, A structural strain method for low-cycle fatigue evaluation of welded components, International Journal of Pressure Vessels and Piping 119 (2014) 39–51. doi:10.1016/J.IJPVP.2014.03.003.

[15] S. Baba, M. Naruoka, Y. Arizumi, Low-cycle fatigue test of welded tubular joints, Journal of the Structural Division 107 (3) (1981) 487–505.

[16] Health and Safety Executive, Review of low cycle fatigue resistance. Research report 207, Tech. rep., BOMEL, Limited, Norwich, UK (2004).

[17] G. J. Vegte, J. Back, J. Wardenier, Low-cycle fatigue of welded structures. Analysis of low-cycle fatigue on tubular T- and X-joints, Tech. rep. (1989).

[18] B. H. Skallerud, O. I. Eide, A. Johansen, J. Amdahl, On the capacity of tubular T-joints subjected to severe cyclic loading, in: 15th International conference on offshore mechanics and arctic engineering (ASME), 1995, pp. 133–142.

[19] R. J. Scavuzzo, T. S. Srivatsan, P. C. Lam, Fatigue of butt-welded steel pipes, ASME publications-PVP (1998) 113–144.

[20] American Welding Society, Structural welding code-Steel ANSI/AWS D.1.1-83.

[21] X. Pei, P. Dong, An analytically formulated structural strain method for fatigue evaluation of welded components incorporating nonlinear hardening effects, Fatigue & Fracture of Engineering Materials & Structures 42 (239-255). doi:https://doi.org/10.1111/ffe.12900.

[22] X. Pei, P. Dong, S. Xing, A structural strain parameter for a unified treatment of fatigue behaviors of welded components, International Journal of Fatigue 124 (2019) 444–460. doi:10.1016/J.IJFATIGUE.2019.03.010.

[23] B. Fekete, New energy-based low cycle fatigue model for reactor steels, Materials & Design 79 (2015) 42–52. doi:10.1016/J.MATDES.2015.04.039.
URL https://www.sciencedirect.com/science/article/pii/S0261306915002216

[24] G. Shi, Y. Gao, X. Wang, Y. Cui, Energy-based low cycle fatigue analysis of low yield point steels, Journal of Constructional Steel Research 150 (2018) 346–353. doi:10.1016/J.JCSR.2018.08.026.
URL https://www.sciencedirect.com/science/article/pii/S0143974X18306199?via{%}3Dihub

[25] H. Itoga, K. Tokaji, M. Nakajima, H.-N. Ko, Effect of surface roughness on step-wise S-N characteristics in high strength steel, International Journal of Fatigue 25 (5) (2003) 379–385. doi:10.1016/S0142-1123(02)00166-4.

[26] H. C. Yildirim, G. B. Marquis, Fatigue strength improvement factors for high strength steel welded joints treated by high frequency mechanical impact, Interna-

tional Journal of Fatigue 44 (2012) 168–176. doi:10.1016/J.IJFATIGUE.2012.05.002.

[27] J. Waalen, S. Berge, Low cycle fatigue of T-tubular joints with in-plane bending loading, in: 24th International Conference on Offshore Mechanics and Arctic Engineering, Halkidiki, Greece, 2005, pp. 211–219.

[28] F. Boge, T. K. Helland, S. Berge, Low cycle fatigue of T-tubular joints with out-of-plane bending loading, in: 26th International Conference on Offshore Mechanics and Arctic Engineering, 2007, pp. 107–115. doi:10.1115/OMAE2007-29351.

[29] M. Hochman, M. Madshus, S. Berge, Low cycle fatigue of T-tubular joints under axial loading, in: 20th International Offshore and Polar Engineering Conference, International Society of Offshore and Polar Engineers, 2010, pp. ISOPE–I–10–479.

[30] G. E. Varelis, T. Papatheocharis, P. C. Perdikaris, S. A. Karamanos, High-strength steel tubular welded joints under extreme loading conditions, in: 26th International Ocean and Polar Engineering Conference, Rhodes, 2016, pp. ISOPE–I–16–425.

[31] G. E. Varelis, T. Papatheocharis, S. A. Karamanos, P. C. Perdikaris, Structural behavior and design of high-strength steel welded tubular connections under extreme loading, Marine Structures (2019) Under review.

[32] American Welding Society, Structural welding code-Steel AWS D.1.1/D1.1M (2004).

[33] DNVGL- RP - C203, Fatigue design for offshore steel structures. Recommended Practice, DNV GL AS (2016).

[34] DNVGL- RP - C208, Determination of structural capacity by non-linear finite element analysis methods. Recommended Practice, DNV GL AS (2016).

[35] ABAQUS, Standards user's manual, Version 2016. Hibbitt, Karlsson and Sorensen, Inc., 1997.

[36] K. Chatziioannou, S. A. Karamanos, Y. Huang, A robust integration algorithm for cyclic plasticity-damage models, Under preparation.

[37] J. L. Chaboche, Time-independent constitutive theories for cyclic plasticity, International Journal of Plasticity 2 (2) (1986) 149–188. doi:http://dx.doi.org/10.1016/0749-6419(86)90010-0.

[38] J. L. Chaboche, On some modifications of kinematic hardening to improve the description of ratchetting effects, International Journal of Plasticity 7 (7) (1991) 661–678. doi:10.1016/0749-6419(91)90050-9.

[39] S. Bari, T. Hassan, An advancement in cyclic plasticity modeling for multiaxial ratcheting simulation, International Journal of Plasticity 18 (7) (2002) 873–894. doi:10.1016/S0749-6419(01)00012-2.

[40] X.-L. Zhao, Design guide for circular and rectangular hollow section welded joints under fatigue loading (2001).

[41] API 2000, Recommended Practice 2A-WSD, Recommended practice for planning, designing and constructing fixed offshore platforms, working stress design (RP 2A-WSD).

[42] European Committee for Standardization, Eurocode 3: Design of steel structures - Part 1-9: Fatigue strength of steel structures. EN 1993-1-9 standard, Brussels, Belgium. (2002).

[43] J. L. Coffin, A study of the effects of cyclic thermal stresses on a ductile metal, Transactions of ASME 76 (1954) 931–950.

[44] S. Manson, Behaviour of materials under conditions of thermal stress., Tech. rep., National Advisory Commission on Aeronautics: Report 1170. Cleveland: Lewis Flight Propulsion Laboratory (1954).